Supporting Information

3D-printed self-sensing magnetically actuated microfluidic chip for closed-loop drug delivery

Peilong Li[#], Yunfan Li[#], Jiajie Zhan, Deng Wang, Ruyu Zhang, Feng Liu*

School of Power and Mechanical Engineering, Wuhan University, Wuhan, Hubei, 430072, China.

*Corresponding author. E-mail: fengliu@whu.edu.cn

[#]These authors contributed equally to this work.

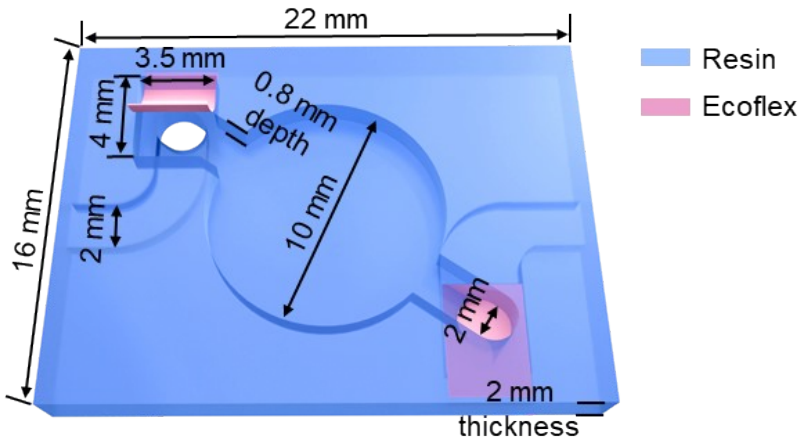

Figure S1. Detailed geometry and dimensions of the 3D-printed microfluidic layer of the SMAM chip. The design features a central pumping chamber (10 mm in diameter, 0.8 mm in depth), inlet/outlet channels (2 mm wide), and integrated seats for the passive flap valves. These dimensions are optimized to achieve a significant stroke volume for effective fluid transport.

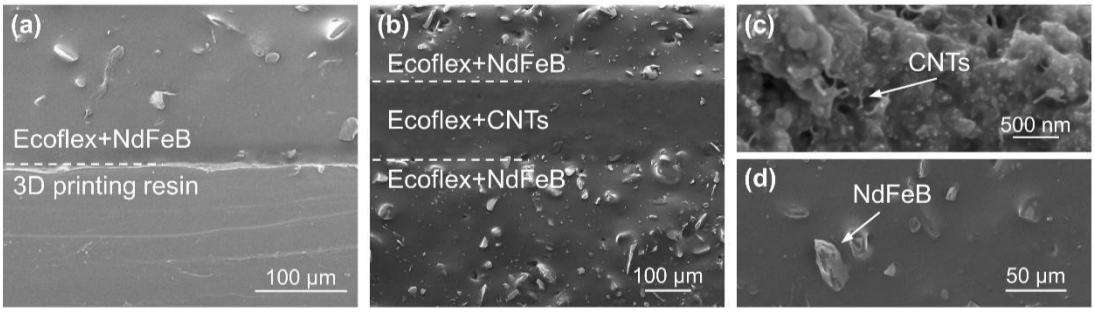

Figure S2. Cross-sectional SEM analysis of the SMAM chip. (a) Image of the tightly bonded interface between the 3D-printed resin body and the magnetic composite film. (b) Cross-section of the composite film, illustrating its sandwich structure composed of a central piezoresistive layer and two outer magnetic layers. High-magnification images showing the dispersion of (c) CNTs and (d) NdFeB microparticles within the Ecoflex matrix.

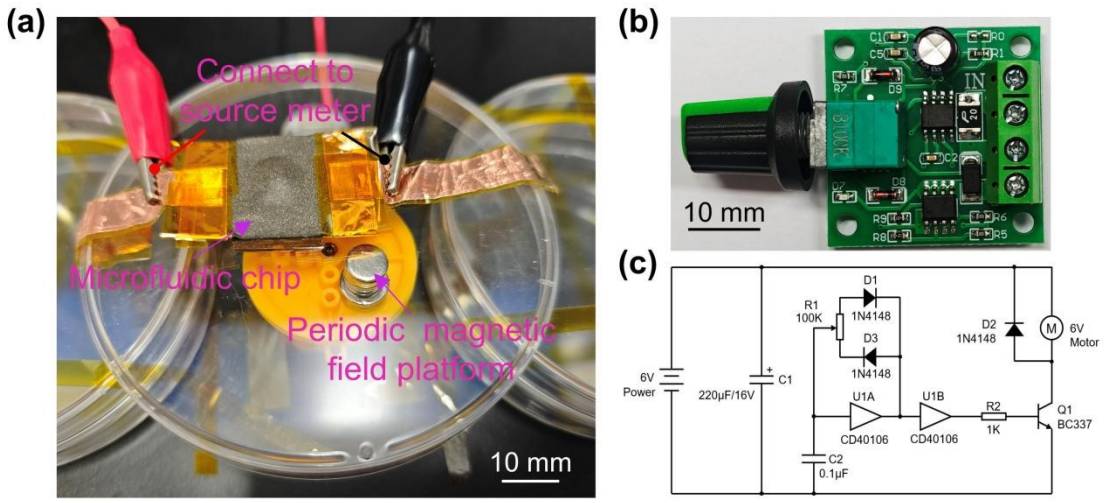

Figure S3. Experimental setup for magnetic actuation and control. (a) Photograph of the SMAM chip positioned on the periodic magnetic field platform. Electrical contacts for real-time piezoresistive sensing are connected to a source meter. (b) Photograph of the custom-built motor speed controller, featuring a potentiometer for adjusting the actuation frequency. (c) Schematic diagram of the speed control circuit.

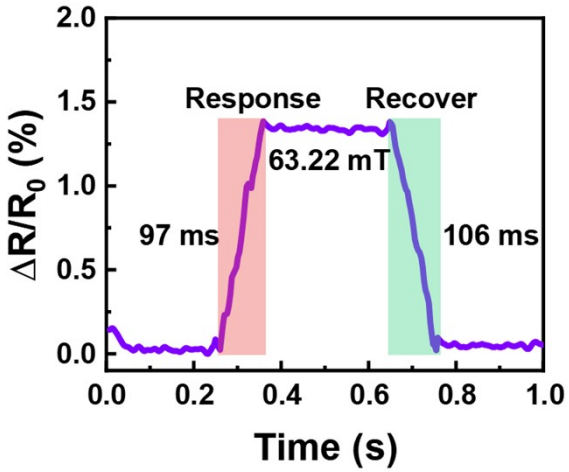

Figure S4. Dynamic response and recovery characteristics of the SMAM chip. The plot shows the temporal profile of the relative resistance change ($\Delta R/R_0$) upon the application and subsequent removal of a **63.22 mT** magnetic field. The sensor exhibits a fast response time of **97 ms** and a recovery time of **106 ms**.

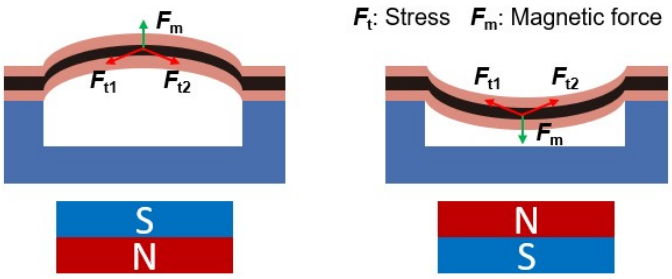

Figure S5. Schematic illustration of the force-balance mechanism on the pump diaphragm leading to sensitivity saturation.

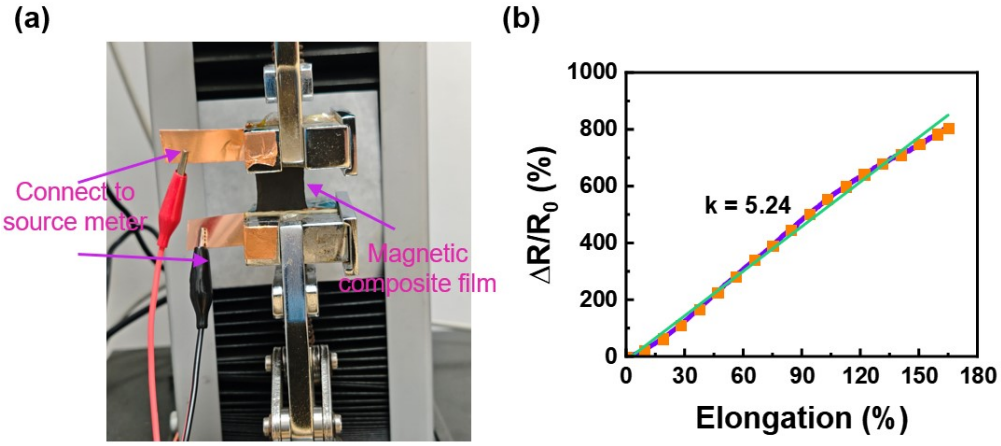

Figure S6. Electromechanical characterization of the magnetic composite film. (a) Experimental setup for measuring the change in resistance of the film under uniaxial tensile strain using a universal testing machine. (b) Relative resistance change ($\Delta R/R_0$) as a function of elongation. The film demonstrates a highly linear piezoresistive response with a gauge factor (k) of 5.24 over a large strain range up to 160%.

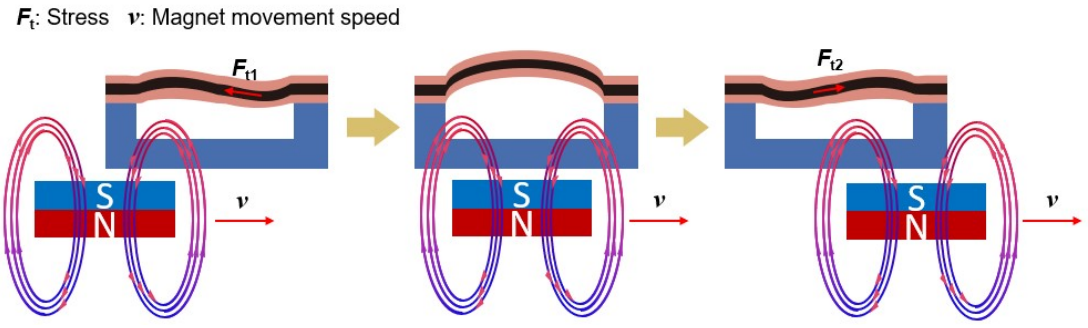

Figure S7. Schematic illustration of the dynamic actuation mechanism. The diagram decomposes the deformation process of the magnetic composite film under a moving magnetic field. As the magnet moves, it exerts a varying magnetic force on the membrane. This spatiotemporal

variation leads to a periodic loading and unloading cycle, which drives the intake and expulsion of fluid and creates the characteristic pulsatile flow profile.

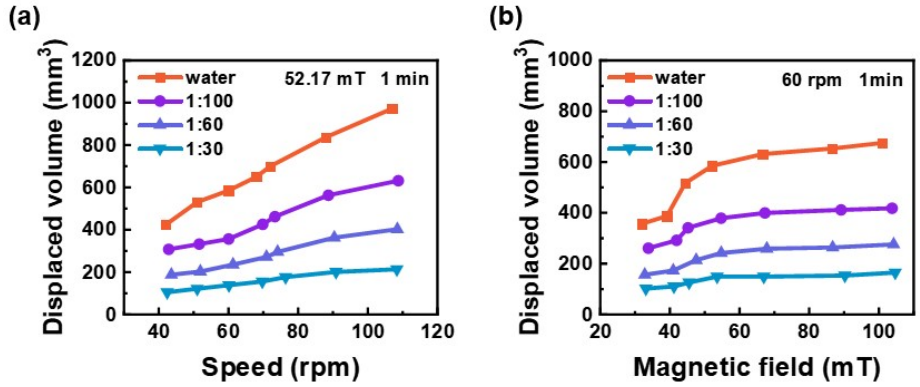

Figure S8. Experimental measurement of the microfluidic chip's pumping performance with fluids of different viscosities. The viscosity was tuned using glycerol-water solutions, volume ratio of glycerol to water is indicated. (a) Cumulative flow rate as a function of actuation frequency. (b) Cumulative flow rate as a function of magnetic field strength.

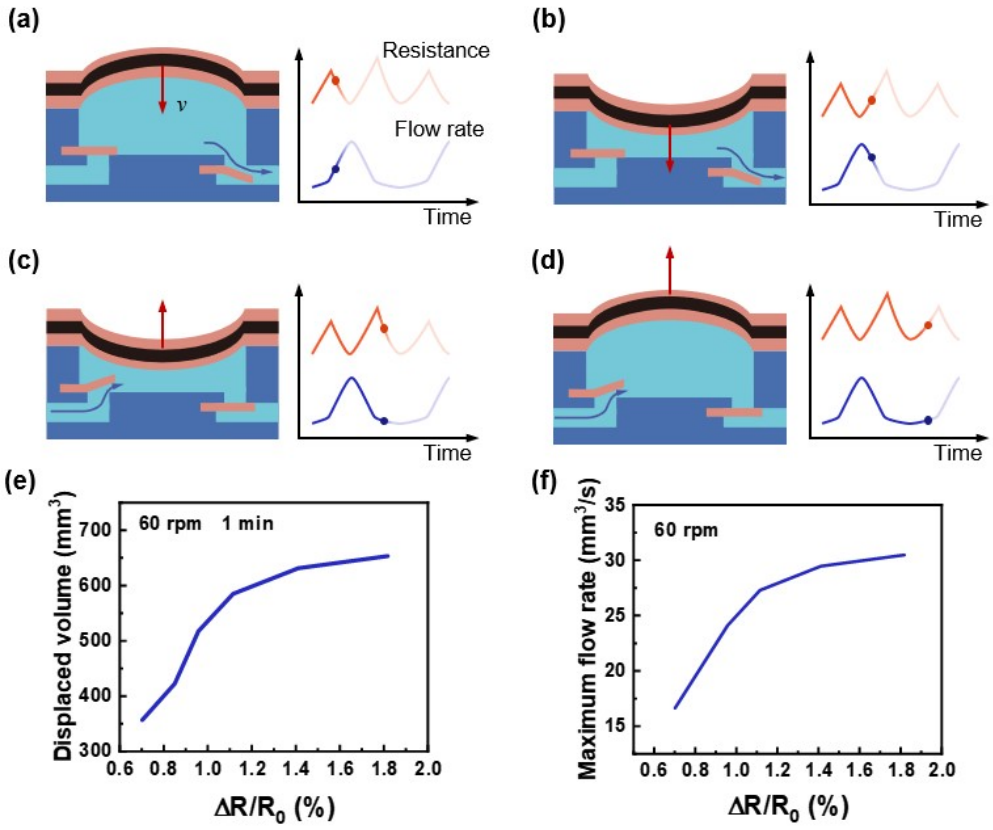

Figure S9. Characterization of the self-sensing mechanism and its correlation with fluidic output. (a–d) Schematic illustrations showing the phase correspondence between the magnetic

membrane deformation, the generated electrical resistance signal, and the instantaneous flow rate during a single pumping cycle. (e) Experimental data plotting the total volume of fluid displaced per minute against the relative resistance change. (f) The relationship between the maximum instantaneous flow rate and the relative resistance change.

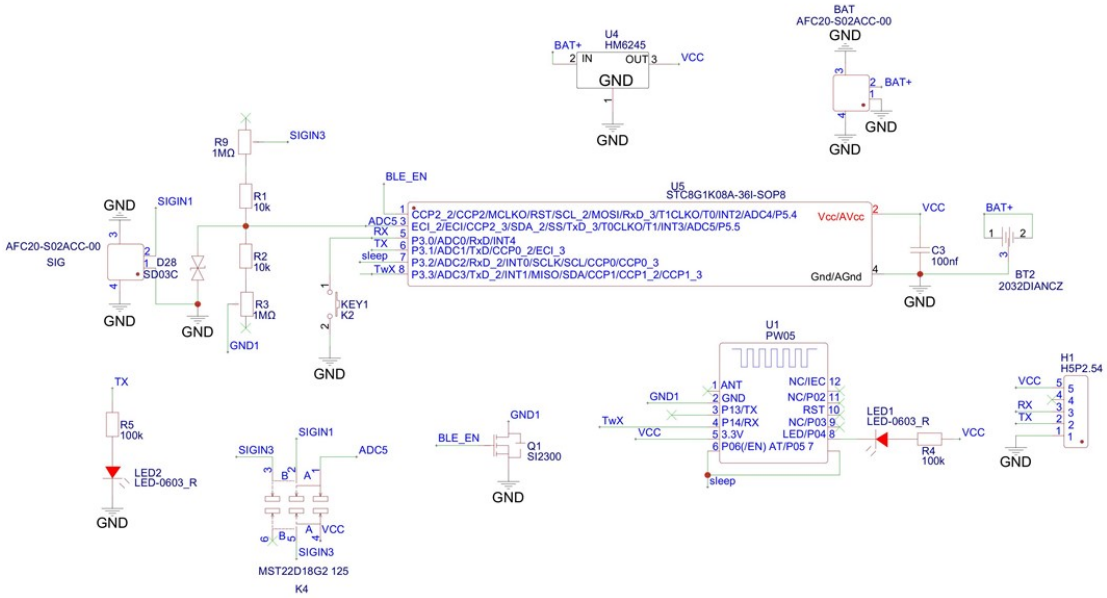

Figure S10. Circuit diagram of the wireless communication module for the SMAM chip.

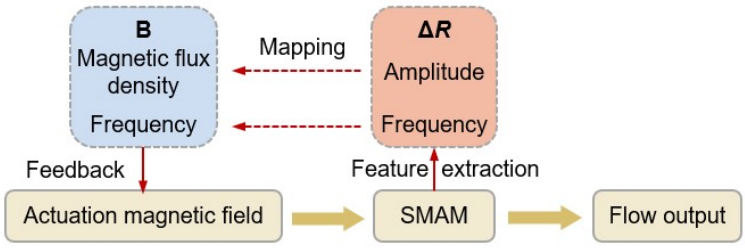

Figure S11. Schematic illustration of the closed-loop flow control logic based on self-sensing feedback. The system extracts the amplitude and frequency features from the resistance change to dynamically modulate the actuation magnetic field parameters, thereby ensuring a stable flow output.

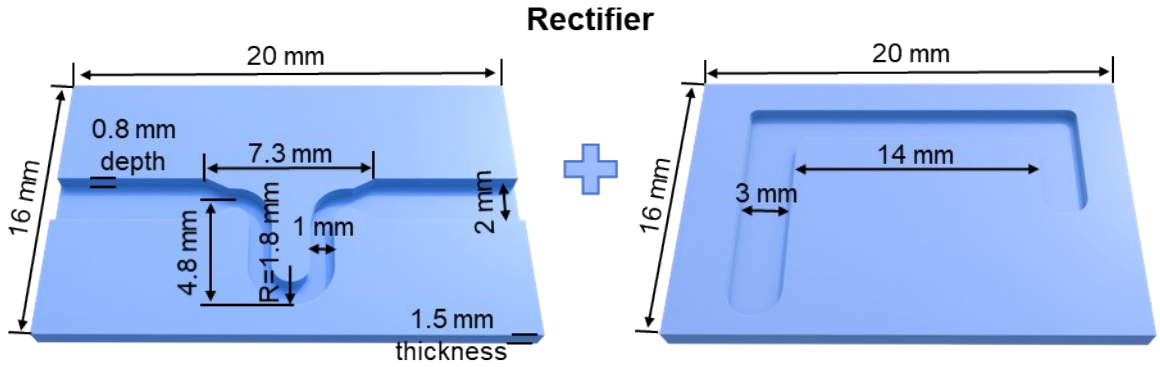

Figure S12. Detailed design and dimensions of the 3D-printed microfluidic rectifier. The device consists of two main components fabricated by SLA 3D printing: a layer containing the primary flow channel (left) and a cover layer with a recessed, sealed side-channel (right). Key features include a 7.3 mm wide interaction chamber in the flow path and a 14 mm long, 3 mm wide side-channel. When assembled with an intermediate flexible membrane, these structures create a fluidic capacitor designed to effectively dampen pulsatile flow.

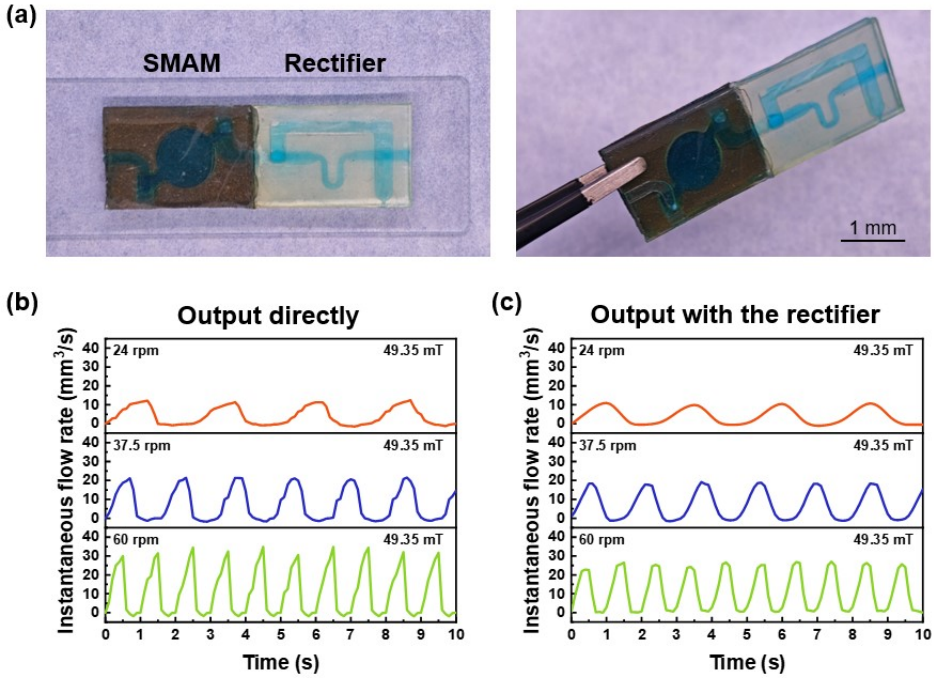

Figure S13. Performance characterization of the flow rectification module. (a) Optical images showing the modular integration of the SMAM chip with the passive microfluidic rectifier. (b) The instantaneous flow rate (IFR) measured directly from the SMAM chip outlet at actuation speeds of 24, 37.5, and 60 rpm. (c) The IFR measured after the fluid passes through the rectifier at the corresponding actuation speeds.

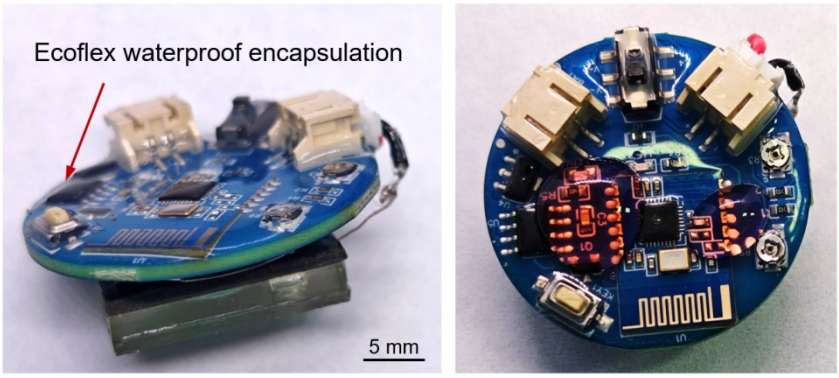

Figure S14. Optical images of the customized PCB with Ecoflex waterproof encapsulation. The circuit board is integrated with the microfluidic chip to enable wireless control and data transmission in fluidic environments.

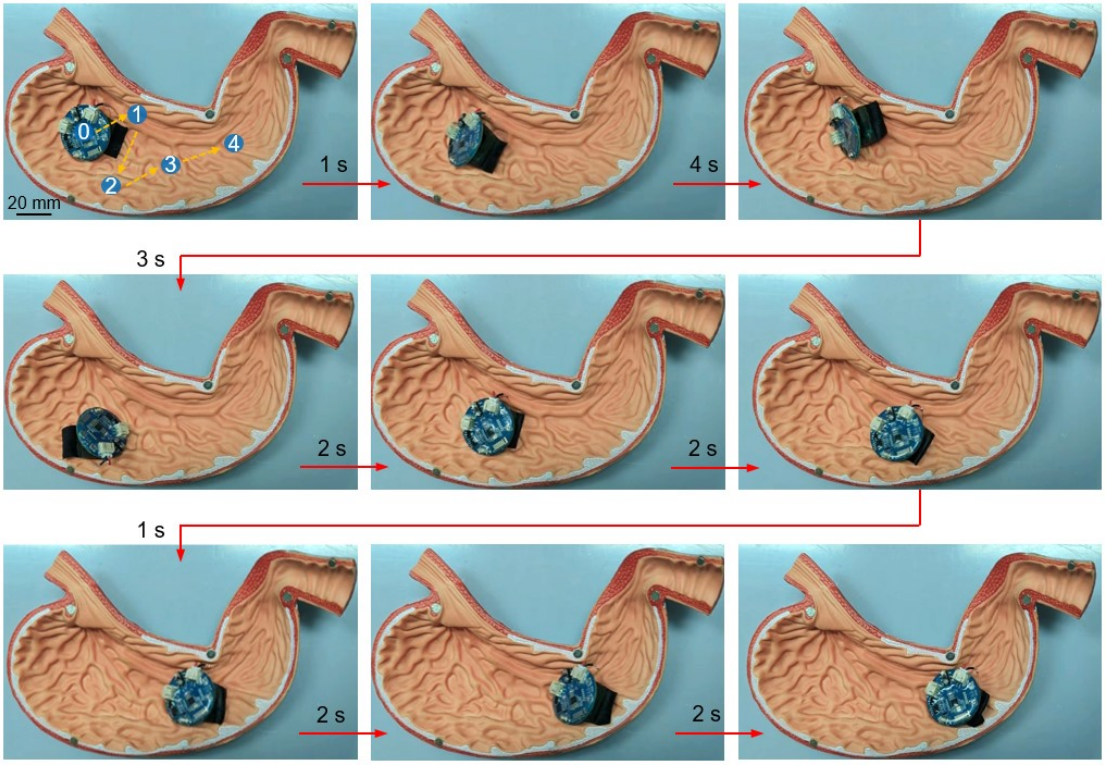

Figure S15. Demonstration of the untethered mobility of the integrated SMAM system. Time-lapse screenshots extracted from **Video S3** showing the SMAM chip, integrated with the wireless PCB module, navigating inside a stomach phantom.

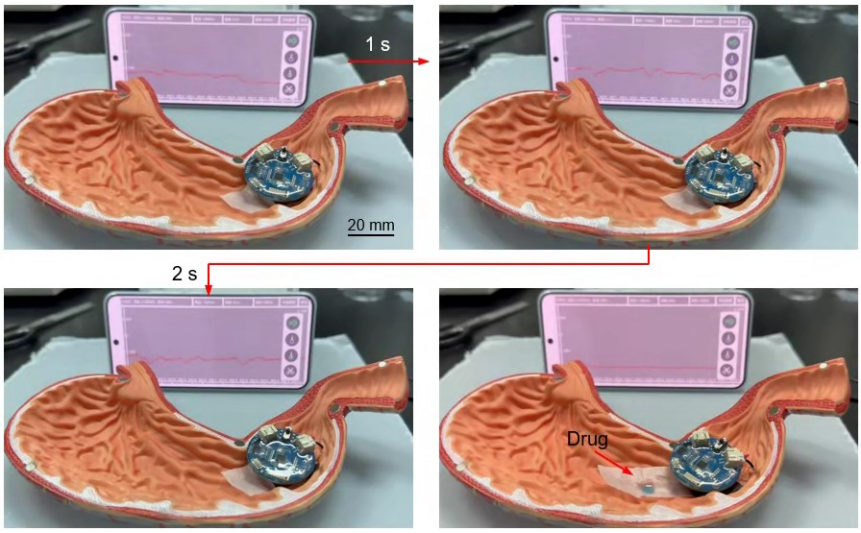

Figure S16. Wireless monitoring of on-demand drug release. Image sequence from **Video S4** illustrating the functional operation of the SMAM chip within a stomach phantom. As the chip executes magnetically actuated drug release, the integrated Bluetooth PCB captures the piezoresistive changes and wirelessly transmits the sensory signals to a mobile device in real-time.

Text S1. Principle of wireless sensing and data transmission

The wireless monitoring functionality is based on converting the dynamic resistance of the SMAM chip (R_s) into a measurable voltage signal. This is achieved using a signal conditioning circuit configured as a voltage divider, which is powered by a stable 3.3 V source (U_{VCC}). In this circuit, the chip (R_s) is placed in the divider network along with two fixed resistors, R_1 = 10 kΩ and R_2 = 10 kΩ. The output voltage (U) across the parallel combination of R_s and R_2 is a function of the chip's resistance, governed by **Equation (S1)**:

$$U = \frac{U_{VCC} \cdot \frac{R_s R_2}{R_s + R_2}}{R_1 + \frac{R_s R_2}{R_s + R_2}} \quad \text{(S1)}$$

This analog voltage (U) is continuously sampled by the analog-to-digital converter (ADC) integrated into the microcontroller unit (MCU). The MCU then calculates the instantaneous chip resistance (R_s) by computationally solving Equation (S1). The rearranged expression used for this calculation is given by **Equation (S2)**:

$$R_s = \frac{R_1 R_2 U}{R_2 U_{VCC} - (R_1 + R_2) U} \quad \text{(S2)}$$

The resulting resistance data, which directly reflects the deformation state of the chip's membrane, is then transmitted wirelessly via an onboard Bluetooth module to a mobile terminal for real-time visualization and data logging.

Table S1. Parameters of the magnetomechanics simulation model.

Material	Parameter	Value
Magnetic substrate	Density	1854 kg/m^3
	Young's modulus	111 kPa
	Poisson's ratio	0.45
	Relative permeability	1.05
	Norm of the magnetization intensity	15915 A/m
Elastic 50A resin	Density	1.01×10^3 kg/m^3
	Young's modulus	2 MPa
	Poisson's ratio	0.49
	Relative permeability	1

Table S2. Parameters of the flow dynamics simulation model.

Material	Parameter	Value
Elastic 50A resin	Density	1.01×10^3 kg/m^3
	Young's modulus	2 MPa
	Poisson's ratio	0.49
Liquid	Density	1×10^3 kg/m^3
	Dynamic viscosity	1.01×10^{-3} Pa·s

Table S3. Performance comparison of the SMAM chip with state-of-the-art microfluidic chips.

Device	Mechanism	Function	Maximum pumping flow rate (μL/min)	Sensitivity (MPa^{-1})	Ref.
SMAM chip	Magnetic drive, Piezoresistive	Pumping, sensing	972	43.1	This work
Micropump	Magnetic drive	Pumping	4.92	NA	[1]
Micropump	Magnetic drive	Pumping	10	NA	[2]
Micropump	Magnetic drive	Pumping	11	NA	[3]
Micropump	Magnetic drive	Pumping	20	NA	[4]
Micropump	Magnetic drive	Pumping	7	NA	[5]
Soft microrobot	Magnetic drive	Pumping	900	NA	[6]
Micropump	Magnetic drive	Pumping	1913.24	NA	[7]
Muscle	Hydraulic	Pumping	174,000	NA	[8]
Folded diaphragm	Magnetic drive	Pumping	180,000	NA	[9]
Soft microrobot	Magnetic drive	Sensing	NA	28.8	[10]

References

[1] Tahmasebipour M, Ebrahimi S, Dehghan M, Anousheh F. A dual-parallel chamber electromagnetic micropump fabricated using 3D printing method from a novel magnetic nanocomposite material. *Int J Precis Eng Manuf*. 2025; **26**(1):209-16.

[2] Binsley JL, Martin EL, Myers TO, Pagliara S, Ogrin FY. Microfluidic devices powered by integrated elasto-magnetic pumps. *Lab Chip*. 2020; **20**(22):4285-95.

[3] Hanasoge S, Hesketh PJ, Alexeev A. Microfluidic pumping using artificial magnetic cilia. *Microsyst Nanoeng*. 2018; **4**(1):11.

[4] Kibar G, Sarıarslan B, Doğanay S, Yıldız G, Usta OB, Çetin B. Novel 3D-printed microfluidic magnetic platform for rapid DNA isolation. *Anal Chem*. 2024; **96**(5):1985-92.

[5] Mi S, Pu H, Xia S, Sun W. A minimized valveless electromagnetic micropump for microfluidic actuation on organ chips. *Sens Actuator A-Phys*. 2020; **301**:111704.

[6] Xiao B, Lin H, Buckner E, Pierce JM, Tosoian JJ, Dong X. Wireless microfluidics-enabled multifunctional miniature soft robots with multimodal locomotion for fluid manipulation. *Device*. 2025; **3**(6):100713.

[7] Li H, Wang W, Xu T, Huang Y, Fang W. High performance electromagnetic micropump with bio-inspired synchronous valves for integrated microfluidics. *Sens Actuator A-Phys*. 2023; **360**:114568.

[8] Davies J, Thai MT, Low H, Phan PT, Hoang TT, Lovell NH, Do TN. Bio-SHARPE: Bioinspired soft and high aspect ratio pumping element for robotic and medical applications. *Soft Robot*. 2023; **10**(6):1055-69.

[9] Lin D, Yang F, Gong D, Li R. Bio-inspired magnetic-driven folded diaphragm for biomimetic robot. *Nat Commun*. 2023; **14**(1):163.

[10] Xu H, Wu S, Liu Y, Wang X, Efremov AK, Wang L, McCaskill JS, Medina-Sánchez M, Schmidt OG. 3D nanofabricated soft microrobots with super-compliant picoforce springs as onboard sensors and actuators. *Nat Nanotechnol*. 2024; **19**(4):494-503.